Gas Processing Journal

Vol. 9, No. 2 2021, pp. 131-148
http://gpj.ui.ac.ir

Research Paper

CFD simulation of an industrial gas condensate electrostatic desalter: a case study

Fatemeh Amini[1], Ali Mohebbi [*2]

[1] Department of Chemical Engineering, Faculty of Engineering, Shahid Bahonar University of Kerman, Kerman, Iran

[2] Department of Chemical Engineering, Faculty of Engineering, Shahid Bahonar University of Kerman, Kerman, Iran

Received: 2022-03-202 Revised: 2022-10-24 Accepted: 2022-11-08

Abstract: A desalter is a process equipment in a gas refinery that removes saline water from natural gas condensate. In this study, to predict the electrostatic desalter performance in Refinery No. 4, South Pars, Iran, a 3D computational fluid dynamics (CFD) simulation considering the population balance model based on Eulerian-Eulerian two-phase flow was performed. The continuity and time-averaged Navier-Stokes equations were solved by the finite volume method. To assess the water droplets' coalescence and consider the role of the electric field under the DC current a User-Defined Function (UDF) was written and compiled to the Fluent. To validate the CFD results, the calculated volume fraction of the water phase was compared with industrial data. Also, two different operating conditions were considered for better evaluation. The main goal was how CFD simulation by using one section instead of the main geometry can solve all complexity of the process. The results showed that between two electrodes, the coalescence of droplets was greater, and also droplets size distribution in the water outlets indicates the percentage of smaller-sized groups was decreased, and the larger size groups gain value.

keywords: Electrostatic desalter; CFD; Population balance model; Droplet coalescence; Eulerian-Eulerian two-phase method

1 Introduction

One of the world's largest gas complexes is the South Pars Gas Complex. South Pars Refinery No.4 produces 170,000 barrels of gas condensate per day; therefore, it is essential to assess the greater purity achievement process.

Saline water pollutes and corrodes pipes, installations, pumps, and other process equipment; therefore, all refineries desalinate crude oil. For this purpose, the applied methods should be economical. To increase the oil purity, this emulsion should be removed. The purpose of desalination is the dissolution of salt types in crude oil by water (Eow & Ghadiri, 2001). A desalination plant includes an electrostatic drum and coalesces tank, in which free water droplets are separated from crude oil and fresh water is mixed with crude oil to decrease salt concentration, which enters the electrostatic desalter (Aryafard, Farsi, & Rahimpour, 2015).

The electric field causes the dispersion of dispersed phase droplets to collide faster, reduces the surface tension of the surface film, increases collision frequency, and integrates the droplets. Many attempts are made by some researchers to introduce new approaches in this context, which would increase the efficiency and purity of crude oil (Hosseinpour, 2016).

Zhang, Basaran, & Wham (1995) run a fundamental assessment of the effects of droplets' coagulation and growth to determine the combined effect of gravitational force and electrostatic force for the first time. They focused more on improving the collision rate, spherical growth, and dispersion by an external electric field. A population dynamics equation was solved to estimate the time needed for distribution and the droplets' average size. Berg, Lundgaard, Besidan, & Sigmond (2002) assessed water droplets' breakage in an electric field in the naphthalene, which served as a function of water conductivity, droplet surface tension, and frequency.

Due to the high volume of water in the oil and the problems, Zeidani and Bahadori (2008) presented a new equation for estimating the optimum feed rate, improving the temperature and viscosity in bipolar desalter and AC current

* Corresponding Author.
Authors' Email Address: [1] F. Amini (aminifateme.af@gmail.com), [2] A. Mohebbi (amohebbi@uk.ac.ir)

http://dx.doi.org/10.22108/GPJ.2022.132949.1116

in the oil fields of Iran and revealed that the bipolar desalter is more beneficial with higher complete dewatering than that of AC desalter. Meidanshahi, Jahanmiri, & Rahimpour (2012) proposed a new mathematical approach based on the bivariate population equation to model the distribution of water droplet size and salt concentration during an electrostatic AC desalter and modeled a two-stage industrial desalination process based on the population equation.

Mhatre and Thaokar (2015) performed an experimental assessment of the symmetric and asymmetric, uniform, and non-uniform electric fields for the electrocoalescence of three emulsions. A conducting phase was dispersed in a dielectric medium and a dielectric phase was dispersed in a phase with high electrical conductivity and another dielectric phase with less electrical conductivity. The electrocoalescence behavior of each emulsion in a non-uniform electrical field was compared with the results of the uniform field.

Further research on developing the population balance model was conducted by Aryafard, Farsi, Rahimpour, & Raeissi (2016) where the class method is selected as a mathematical technique for solving the bivariate population model and they developed the model with the assumption that the data of the industrial desalination unit are evaluated. Rossi et al. (2017) devised a first-principle mathematical model for separating water from oil in water-in-oil emulsions in electrostatic coalescer units. The coalescence of the emulsion droplets is considered in the dynamics of the mathematical model. Their simulation results correspond with the industrial data, indicating that this model is applicable in design, unit behavior prediction, and optimization. At first Ramirez-Argaez, Abreu-Lopez, Gracia-Fadrique, & Dutta (2021) solved the collision time of two droplets in a (W/O) emulsion numerically. The main parameters like electric field strength, water content, temperature, and droplet size on the collision time were investigated.

Ranaee, Ghorbani, Keshavarzian, Ghazaeipour, Riva & Guadagnini (2021) investigated the performance of a crude-oil desalting/demulsification system. They considered three methods to achieve their goal: 1) Global Sensitivity Analysis (GSA), 2) Machine learning and 3) rigorous model discrimination/identification criteria. Dhandhi, Kumar Chaudhari & Kumar Naiya (2022) discussed effective factors on emulsions stability and studied chemical natural demulsifiers derived from a natural source.

Ahmadi, Khormali & Khoutoriansky (2022) studied the effects of space velocity, temperature, demulsifier content, and wash water ratio on the performance of demulsification of water-in-crude oil emulsions. They also used an electrostatic desalting pilot plant to perform their experiments.

In this study, a CFD simulation was run based on the Eulerian multiphase, and the collision and the coalescence of droplets were considered in this simulation. Also, this simulation was validated once with moisture content and intensity of the electrostatic field and a second time without these variables. It was concluded that due to the sophistication of the desalination phenomenon, all main variables should be considered.

Although some one-dimensional mathematical modelings for plug flow regimes have been performed for electrostatic desalters, more studies for industrial cases taking into account turbulent flow inside the desalter need to be done. Due to non-sufficient studies run on the desalinization of gas condensates and its importance, and few studies on electrostatic desalination with DC current, the objective of this study is to simulate the desalter of the South Pars Refinery No. 4 by using computational fluid dynamics. The content of water and salt in the outlet of gas condensates from the desalter is calculated as the measurement criterion. The role of different parameters like the electric field, electrostatic forces and their role in the water droplets coalescence, and different operating conditions are assessed on the simulation results of the desalinization process of gas condensates.

2 Process description and industrial measurements

In the gas condensate desalting plant, the condensate is entered into a pre-flash drum, which is a three-phase separator. The condensate in this separator is dehydrated and degassed. After preheating, fresh water and the condensate is mixed inside the mixing valve to dilute the brine and then are entered into desalter, where water and condensate are separated, and finally, the condensate is transferred to the condensate stabilizer tower. Figure 1 shows the schematic diagram of a section of the explained desalting unit.

The required physical properties of continuous and dispersed phases related to the 4th South Pars Refinery and the industrial measurement of the electric field are tabulated in Table 1. The mass flow rates of water and salt in the inlet and outlet flows of the desalter together with the corresponding operating conditions for two different operating conditions are tabulated in Tables 2 and 3.

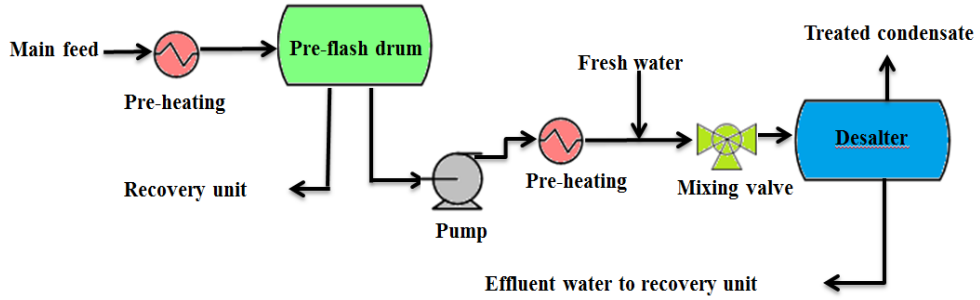

Figure 1. Schematic view of device arrangement in a section of desalting unit

Table 1. Physical properties of the liquid phases in the desalter

Parameter	
Aqueous viscosity (Pa.s)	0.001
Organic viscosity (Pa.s)	0.00035
Aqueous density (kg/m^3)	997
Organic density (kg/m^3)	707
Constant of dielectric continuous phase	2.5
Applied electric field (V/m)	100

Table 2. Operating conditions for the desalter, (case A)

	Gas condensate inlet	Gas condensate outlet	Water outlet
T (℃)	59.1	59.1	59.1
(kPa g) Pressure	37.1	37	37
Total mass flow rate (kg/h)	3319.7	3307.6	12.1
Water mass flow rate (kg/h)	13.9	1.9	12.1
Salt mass flow rate (kg/h)	0.082	0.0047	0.077

Table 3. Operating conditions for the desalter, (case B)

	Gas condensate inlet	Gas condensate outlet	Water outlet
T (℃)	58	58	58
(kPa g) Pressure	37.6	37	37
Total mass flow rate (kg/h)	4272	4024.7	247.1
Water mass flow rate (kg/h)	249.5	2.4	247.1
Salt mass flow rate (kg/h)	0.30	0.023	0.577

3. Methodology

In this study, the Eulerian-Eulerian method along with the population balance equation for water droplets was run to solve the flow governing equations. The momentum equation included buoyancy, drag, turbulence, and lift forces. The simulation was run as 3D, steady-state, turbulent flow, incompressible flow, isothermal, and without mass-heat transfer.

3.1 Continuity equation

The continuity equations in time-averaged form for incompressible flow and steady-state are expressed as follows (Versteeg and Malalasekera, 2007; White and Majdalani, 2006):

$$\nabla.(\alpha_c U_c) = 0 \quad (1)$$

$$\nabla.(\alpha_d U_d) = 0 \quad (2)$$

where c subscript is the continuous phase, d is the dispersed phase and α is the volume fraction and U is the velocity vector.

3.2 Momentum equations

These equations in their time-averaged form for the steady-state, incompressible turbulent flow are expressed as follows (White and Majdalani, 2006; Soo, 1999):

$$\rho_c\left[\nabla.(\alpha_c U_c U_c)\right] = -\alpha_c \nabla P + (\mu_c + \mu_t)\nabla^2(\alpha_c U_c) + S_{M,c} \quad (3)$$

$$\rho_d\left[\nabla.(\alpha_d U_d U_d)\right] = -\alpha_d \nabla P + (\mu_d + \mu_t)\nabla^2(\alpha_d U_d) + S_{M,d} \quad (4)$$

where P is the pressure, S_M is the source term due to the body forces in the desalter, the body forces consist of gravity, buoyancy, drag, turbulence dispersion, and electrostatic forces. μ and μ_t are molecular and turbulent viscosity, respectively. μ_t is obtained from the following equation according to the realizable $k-\varepsilon$ model (ANSYS Fluent 16 User's Guide, 2006):

$$\mu_t = \rho C_\mu \frac{k^2}{\varepsilon} \quad (5)$$

The buoyancy force for the dispersed phase is expressed as follows (ANSYS Fluent 16 User's Guide, 2006)

$$F^{buo}{}_{d} = \alpha_d(\rho_d - \rho_o)g \quad (6)$$

where, ρ_0 is the reference density, because the continuous phase density is considered as a reference, the buoyancy force is zero for the continuous phase.

The drag force exerted on the dispersed phase is expressed as Eq. 7 (ANSYS Fluent 16 User's Guide, 2006):

$$F_d^{drag} = \frac{1}{2}\rho|U_{rel}|U_{rel}A_pC_d \quad (7)$$

where U_{rel} is the relative velocity between the phases, A_p is the projected frontal area of the droplet, and C_d is the drag coefficient.

The lift force depends on the relative velocity and the continuous phase velocity curl and for the dispersed phase it is expressed as follows (ANSYS Fluent 16 User's Guide, 2006):

$$F_d^{lift} = \alpha_d\rho_c C_L\left(U_c - U_D\right)\times(\nabla\times U_c) \quad (8)$$

where the lift coefficient is C_L and U is the velocity.

Droplets are dispersed due to interactions in turbulent flow, which is considered a turbulent force. This force depends on the momentum fluctuations and the volume fraction gradient in the continuous phase. The turbulence force of the dispersed phase is expressed as follows (ANSYS Fluent 16 User's Guide, 2006):

$$F_d^{td} = -C_{TD}\rho_d k_d \nabla\alpha_d \quad (9)$$

where C_{TD} is the dispersion coefficient of turbulence and k_d is the turbulence kinetic energy of the dispersed phase. This force in the continuous phase is equal to the dispersed phase with the opposite sign.

If the water droplet size > the diameter of the droplets expressed by the Stokes equation, the weight effect is greater than the drag force, and the droplet falls to the bottom and separates from the condensate (Aryafard, Farsi, & Rahimpour, 2015; ANSYS Fluent 16 User's Guide, 2006):

$$d_{Stoke} = \left(\frac{18\mu_o v_v}{g(\rho_w - \rho_o)}\right) \quad (10)$$

where v_v is the velocity of the droplet and μ_o is the viscosity of the continuous phase.

To increase the efficiency of the desalination process, the electrostatic force should be able to coagulate small droplets and enlarge their diameter as Stoke's diameter. The electrophoretic force, which includes attractive and repulsive forces, is generated in a uniform voltage field between the charged droplets and the electrodes (Hosseinpour, 2016). Because the geometry is an electric field type with uniform DC, the electrophoretic force is more important than other electrostatic forces. This force F_e is calculated by Eq. 11, (Hosseinpour, 2016):

$$F_e = c\pi^3\mu_o\varepsilon_o r^2E^2e^{\left(\frac{-\sigma_o t}{\varepsilon_o}\right)} \quad (11)$$

here, the intensity of the electric field is E, the droplet radius is r, μ_o, ε_o and σ_o are, the viscosity, permittivity coefficient, and the surface tension of reference (continuous phase), respectively.

In Eqs. 3 and 4, the $S_{M.C}$ and $S_{M.d}$ are expressed as follows (ANSYS Fluent 16 User's Guide, 2006):

$$S_{M.C} = F_c^{buo} + F_c^{drag} + F_c^{lift} + F_c^{td} + F_{ec} \quad (12)$$

$$S_{M.d} = F_d^{buo} + F_d^{drag} + F_d^{lift} + F_d^{td} + F_{ed} \quad (13)$$

3.3 Droplet governing equations

One of the most commonly applied models to represent the growth and breakage rates of dispersed droplets is the population balance equation, which describes the hydrodynamics of a dispersed phase moving in a continuous phase. This equation takes into account droplets' breakage and coalescence and change in the distribution of droplets (Coulaloglou and Tavlarides, 1977).

The equation of continuity for the *i*-size group in steady-state is expressed as follows (Sadeghi, Mohebbi, & Baniasadi, 2011):

$$\rho_d\left[\nabla.\left(\alpha_{d,i}U_d\right)\right] = S_i \quad (14)$$

where, the source term, S_i expresses the mass transfer to the *i*-size group because of the droplets breakage and coalescence processes. The equation is written for all size groups. The sum of the volume fraction of all the size groups should equal the dispersed phase volume fraction (Sadeghi, Mohebbi, & Baniasadi, 2011):

$$\sum \alpha_{d_i} = \alpha_d \quad (15)$$

The size groups volume fraction is obtained as follows (Sadeghi, Mohebbi, & Baniasadi, 2011):

$$\alpha_{d_i} = \alpha_d f_i \quad (16)$$

where, f_i is the dispersed phase fraction for the *i*-size group. If Eq. 16 is inserted in Eq. 14, then, the *i*-size group continuity equation is obtained in steady-state. Following this, the number density of the *i*-size group and the droplets volume of the *i*-size group are related to the volume fraction of the dispersed phase by applying Eq. 17. Therefore, the population balance equation is related to the *i*-size group continuity equation (Sadeghi, Mohebbi, & Baniasadi, 2011):

$$n_i v_i = \alpha_d f_i \quad (17)$$

$$\rho_d \left[\nabla.(n_i U_d)\right] = \rho_d \left[\nabla.(\alpha_d f_i U_d)\right] = S_i' = B_B - D_B + B_c - D_c \quad (18)$$

where the droplets number density is n_i and the volume of droplets in the i-size group is v_i .

In Eq. 18, B_B is the *i*-size group birth rate expressed as follows by larger droplets breakage (Sadeghi, Mohebbi, & Sarrafi, 2010):

$$B_B = \sum_{j=i+1}^{N} g\left(v_j : v_i\right) n_j \quad (19)$$

where N is the total number of size groups and the characteristic velocity for breakage of droplets is $g\left(v_j : v_i\right)$.

D_B is the droplets' death rate in the *i*-size group due to breakage to smaller droplets expressed as follows (Sadeghi, Mohebbi, & Sarrafi, 2010):

$$D_B = g_i n_i \quad (20)$$

and B_c is the birth rate of *the i*-size group due to droplets coalescence of *j*-size and k-size groups expressed as follows (Sadeghi, Mohebbi, & Sarrafi, 2010):

$$B_c = \frac{1}{2}\sum_{j=1}^{i}\sum_{k=1}^{i} Q_{jk} n_j n_k \quad (21)$$

and the *i*-size group death rate is D_c due to coalescence with other droplets expressed as follows (Sadeghi, Mohebbi, & Sarrafi, 2010):

$$D_C = n_i \sum_{j=1}^{N} Q_{ij} n_j \quad (22)$$

where, Q_{ij} is the characteristic velocity for coalescence of droplets.

As observed in Eq. 23, the applied electric field is less than that of the critical electric field of each droplet, so the breakage and the loss of the droplet should be ignored. Therefore, the population balance equation is expressed as Eq. 24. In Eq. 23, λ is the interfacial tension between water and condensate, ε_0 is the vacuum permittivity, ε_1 is the dielectric constant of the continuous phase, and *r* is the droplet radius.

$$E_c = 0.64\left(\frac{\lambda}{2\varepsilon_o \varepsilon_1 r}\right) \quad (23)$$

$$\rho_d \left[\frac{\partial(n_i)}{\partial t} + \nabla.(n_i U_d)\right] = \rho_d \left[\frac{\partial(\alpha_d f_i)}{\partial t} + \nabla.(\alpha_d f_i U_d)\right] = S_i' = B_c - D_c \quad (24)$$

$$d_s = \frac{1}{\sum_i \frac{f_i}{d_i}} \quad (25)$$

Eq. 18 is solved to determine the scalar variable f_i and after that, the mean diameter is calculated by Eq. 25 and is applied in calculations of the drag force in the momentum equation. In Eq. 25, d_i is the droplet diameter of the *i*-size group and d_s is the mean diameter (Sadeghi, Mohebbi, & Sarrafi, 2010):

3.4 Droplets coalescence

In general, the adhesion coefficient is defined as the number of droplets collisions multiplied by their collision efficiency expressed as follows (Hosseinpour, 2016; Akbarian Kakhki, Farsi, & Rahimpour, 2016):

$$Q_{jk} = K\pi\left(d_k + d_j\right)^2 V_{jk} e_{jk} \quad (26)$$

where K is an empirical coefficient for the relation between the two sides of the equation, *d* is the diameter of the droplet, V_{jk} is the relative velocity of the *j* and *k* droplets affected by the gravitational force, and e_{jk} is the droplet collision efficiency. The V_{jk} equation is expressed as follows (Hosseinpour, 2016; Akbarian Kakhki, Farsi, & Rahimpour, 2016):

$$V_{jk} = \frac{2\left(\frac{\mu_d}{\mu_c}+1\right)\left|\rho_d - \rho_c\right| r_j^2 \left(1-\frac{v_k}{v_j}\right)^2 g}{3\left(3\frac{\mu_d}{\mu_c}+2\right)\mu_c} \quad (27)$$

where, v_k and v_j are, the volume of k and j droplets, respectively.

As there is no equation for direct current (DC) to calculate the collision efficiency under the electric field influence, the equations of alternating current (AC) with the application of a correction coefficient are applied here when defined as follows:

$$E_{DC} = \frac{E_{AC}}{\sqrt{2}} \quad (28)$$

The equation of vertical alternating collision efficiency with correction coefficient for direct current is expressed as follows (Hosseinpour, 2016; Akbarian Kakhki, Farsi, & Rahimpour, 2016):

$$e_{jk} = \frac{0.14Q_E + 0.1}{Q_E + 0.3} \quad (29)$$

where the electric field intensity is Q_E in the collision of polarized droplets expressed as follows (Hosseinpour, 2016; Akbarian Kakhki, Farsi, & Rahimpour, 2016):

$$Q_E = \frac{2\frac{v_k}{v_j}\Delta\rho\left(1-\frac{v_k}{v_j}\right)gd_j}{3\varepsilon\left(1+\frac{v_k}{v_j}\right)^2 {E_0}^2} \quad (30)$$

where E_0 is the applied electric field and ε is the dielectric constant of the continuous phase.

3.5 Geometry

The geometry of the desalter corresponding to the Refinery No. 4 in the South Pars is shown in Figure 2. In its main dimensions, the desalter is a horizontal cylinder and also has 39 cathodes and 39 anodes. The distance between each pair of electrodes is 0.15 m. The inlet is located on the bottom of the desalter and is connected to two parallel distribution pipes. Each one of the pipes has 100 holes of 0.025 m and 96 holes of 0.015 m diameter and then water and condensate emulsions through these holes fill the desalter space from bottom to top. At the outlet, there is a half-pipe with 11.1 m long and 157 holes. The diameter of each hole is 0.025 m, and through this half-pipe, the salt-free condensates are collected.

The first restriction of this CFD simulation is the complexity of geometry and a large dimension difference in different parts of the geometry, like a large difference between inlets and outlet diameters and own desalter diameter, which needs large grid numbers. Applying the main geometry is time-consuming and inappropriate; moreover, the geometry symmetry cannot be applied because of the large number of grids. It is not possible to simulate two-dimensional due to the fluid distribution in the inlet. Here, by considering the simplified assumptions, a section of the desalter is simulated (Figure 3) where a pair of electrodes, three inlet holes of emulsion and two outlet holes at the top of the desalter for gas condensates and two outlet holes at the bottom for water droplets are embedded. Table 4 gives the simulated section dimensions of the electrostatic desalter. The length of the desalter is 1.153 m. According to Figure 2, the vertical axis is the y-axis. Also because only one section of the desalter is simulated, the flow rates are changed and adjusted in relation to this section.

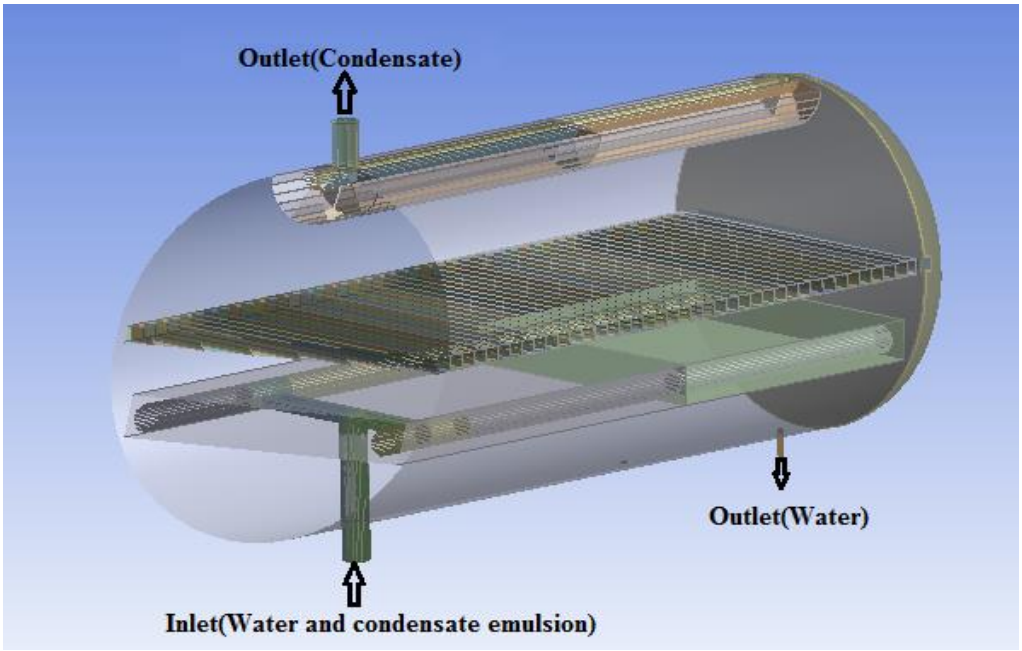

Figure 2. The original geometry of the desalter

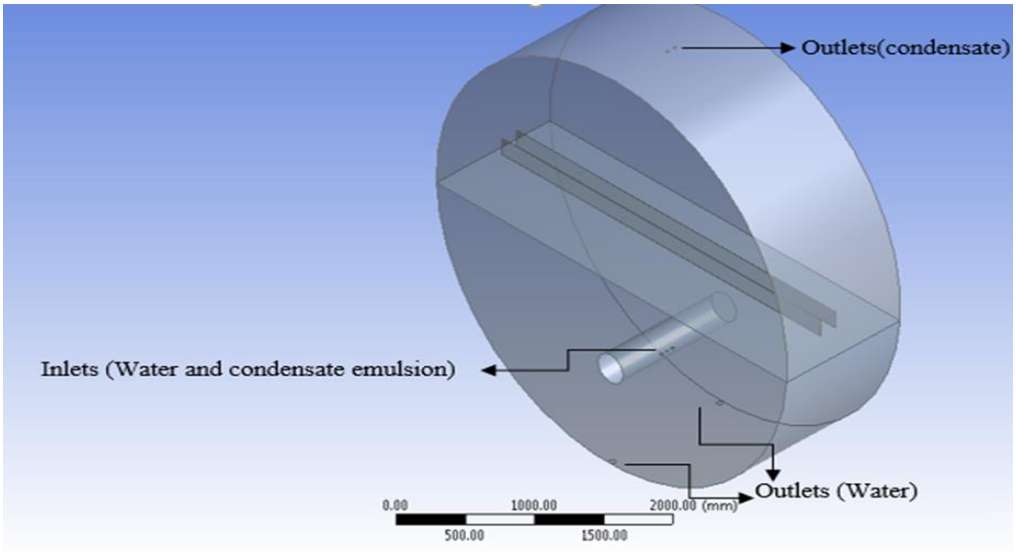

Figure 3. Simulated section of electrostatic desalter

Table 4. The dimensions of simulated section of electrostatic desalter

	Cylinder	Inlet 1 (2 holes)	Inlet 2 (1 hole)	Gas condensates outlet	Water outlet
Diameter(m)	1.8	0.025	0.015	0.025	0.051
Length(m)	1.153	-	-	-	-

3.6 Boundary conditions

The outlet pressure was considered as boundary conditions for both water and condensate outlets, which increases the convergence rate. Also at the inlet, the velocity boundary condition is applied and the desalter is divided into two equal sections for ease, so the number of computational grids decreases and the quality of grids increases, which are then connected by applying the interface boundary condition. The no-slip condition is applied in the walls of the electrode sheets and the desalter body as well. Enhanced Wall Treatment is applied to model the flow near the wall, where the y+ value is calculated to be in the range. Near the electrodes and walls, y+ values were about 70 and 200, respectively. The velocity at the inlet is calculated for the simulated section and inlets 1 and 2, which were 0.99 and 1.64 m/s, respectively, and inlet 1 consists of two holes with the same dimensions. The relative pressure in the outlets of condensate and water is considered to be 37 bar.

3.7 Method of solution

The desalination process is assessed in a steady state. The volume fraction of the dispersed phase is obtained by solving the transport, momentum, Realizable $k-\varepsilon$ turbulent model, and population balance equations simultaneously, in the ANSYS Fluent 16 S/W environment, and the residual values of the parameters were considered to be 0.001. The SIMPLE algorithm was used for pressure-velocity coupling calculations and the second-order upwind method was applied for the discretization of momentum equations. Because of the complexity of geometry and the big dimensional difference between inlets and outlet holes with desalter size, we applied the multizone method with Hexa type for mesh geometry. The multizone method generates a hexahedral mesh where possible and fills the remaining region with unstructured mesh in an automatic manner.

In this study, for operating conditions B (Table 3), to test the grid independency, three different grids with cell numbers 1033404, 1052000, and 1106410 were applied. A comparison of the calculated volume fraction of the dispersed phase with industrial data indicated that error percentages for the mentioned grids were 15, 14, and 10 %, respectively. Therefore, 1052000 cells were selected to ensure the grid independency solution.

The population balance model parameters consist of the number of size groups, each group size, the droplets volume fraction, and kernel types, including growth, loss, aggregation, and so on. Increasing the number of size groups causes a better distribution of droplets. In this simulation, a diameter distribution for water droplets at the inlet was assumed. The number of size groups was assumed 5, 10, and 20 and then assessed. When the size groups of 5 were applied, all the inlet droplet sizes should be considered only in one size group. Even with considering the (K) experimental coefficient, in Eq. 31, it would not be logical if the inlet of the desalter gets close to the maximum diameter, and even when applying the number of size groups, 20, the calculation time would increase drastically; thus, the number

of size group 10 was applied. The minimum diameter was 50 µm and the maximum was 500 µm. The assumed size group distribution of droplets at the inlet is tabulated in Table 5 and shown in Figure 4. Moreover, due to the lower applied electric field compared to the critical electric field, it is possible to avoid droplet breakage in electrostatic desalination. To calculate the droplet coalescence rate, a UDF was applied where the experimental K coefficient in Eq. 31 was 0.005. The electrostatic field was applied on the electrode plate surface and the coalescence rate of the second phase (droplets) was calculated under the electrostatic field.

Table 5. The assumed droplets size distribution at the inlet

Size group (i) number	1	2	3	4	5	6	7	8	9	10
Size group (µm)	50	100	150	200	250	300	350	400	450	500

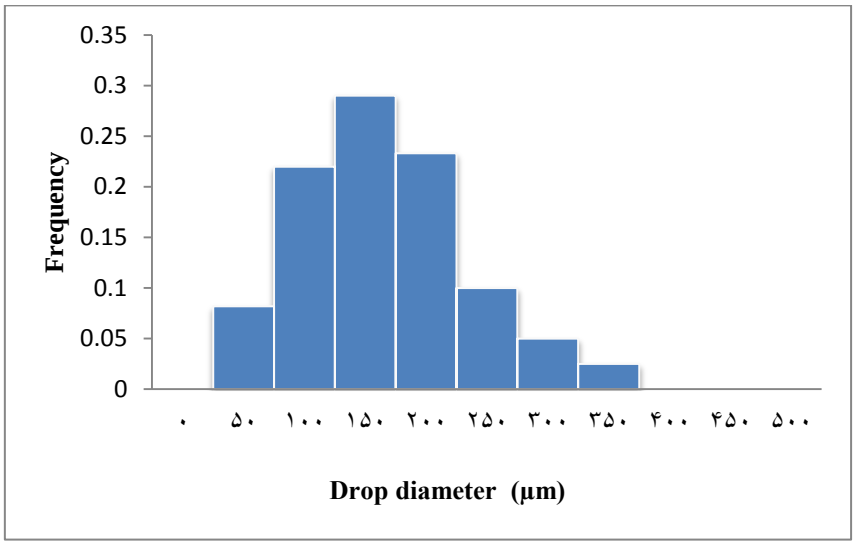

Figure 4. The assumed distribution of droplets size at the inlet

4. Results and discussion

To validate the CFD simulation results, the industrial data of the volume fraction of the water phase was applied at the outlet. To achieve the required accuracy for CFD results, the residual values for convergence of solution were considered to be 10^{-3}. In Table 6 the industrials data and the simulation results are compared for the volume fraction of water at the outlet of condensate for both the operating (A and B) conditions. The water phase volume fraction was used as a measure of separation efficiency in this simulation. The differences between industrials data and simulation results for operating conditions A and B were 2.5 and 11.9 %, respectively, indicative of simulation validity.

Table 6. Comparison of the industrial data with simulation results for the water volume fraction at the outlet of gas condensate for both operating conditions.

Parameters	operating conditions A	operating conditions B
Experimental data	0.0004	0.00042
Simulation results	0.00039	0.00037
Error (%)	2.5	11.9

4.1 Contour of flow velocity

The flow velocity contours in the desalter at the same surface are shown in Figures 5 and 6 for operating conditions A and B, respectively. The flow at the inlet is turbulent, the emulsion, rotating around the inlet and filling the total desalter space. There exists a maximum velocity in the space between the plates and near the cylinder walls, and the velocity is low in the walls. Two different operating conditions are considered, and the simulation results are similar in both conditions, indicative of simulation correctness.

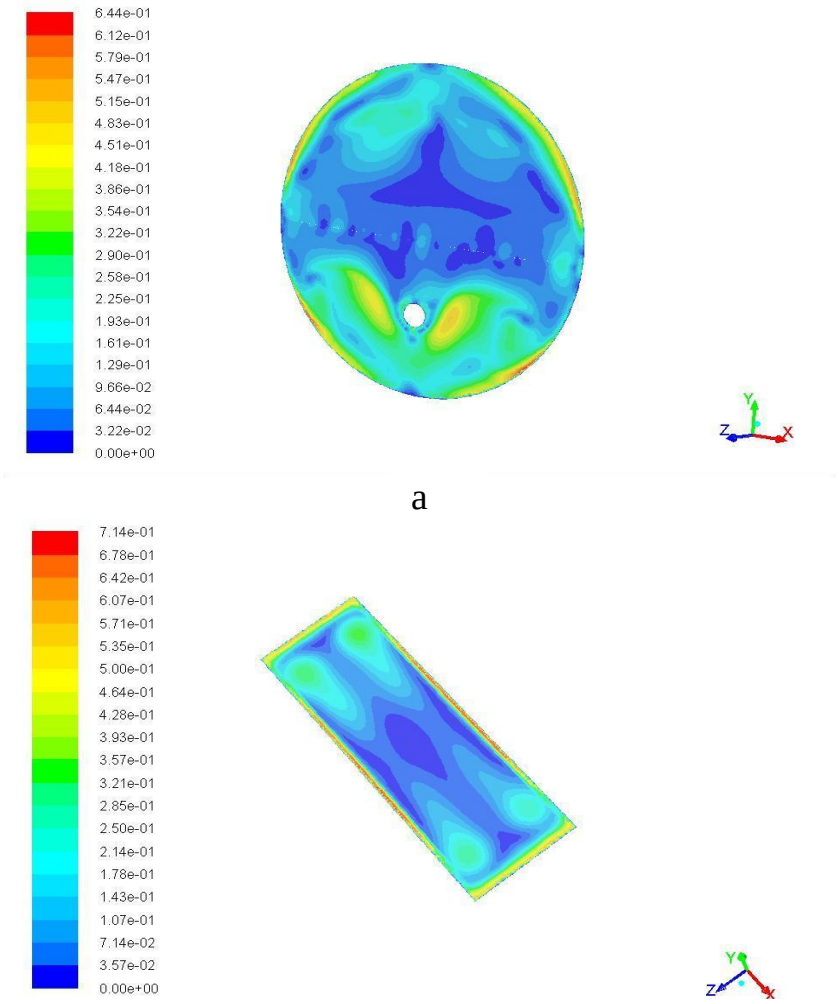

Figure 5. The flow velocity pattern for operating con s A at (a) iso-surface Z=0.56 m (b) iso-surface Y=0.5 m

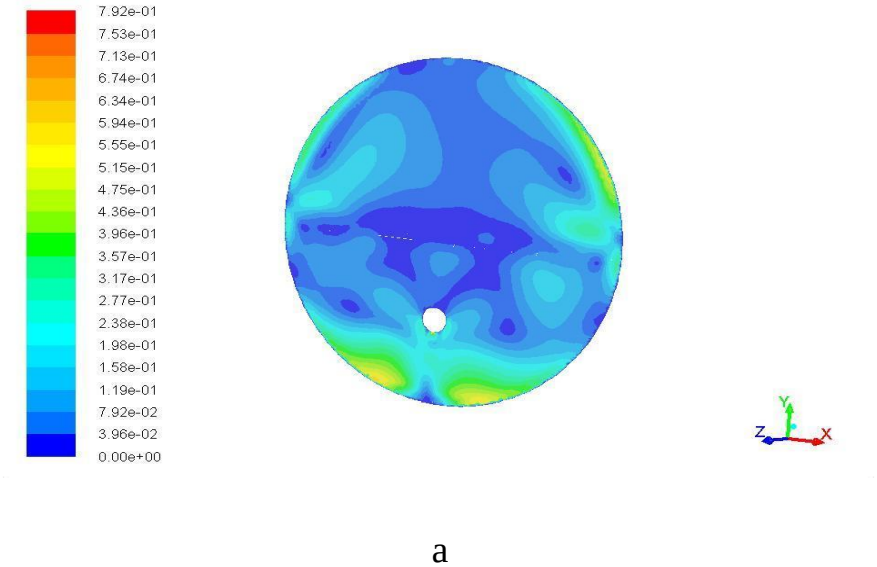

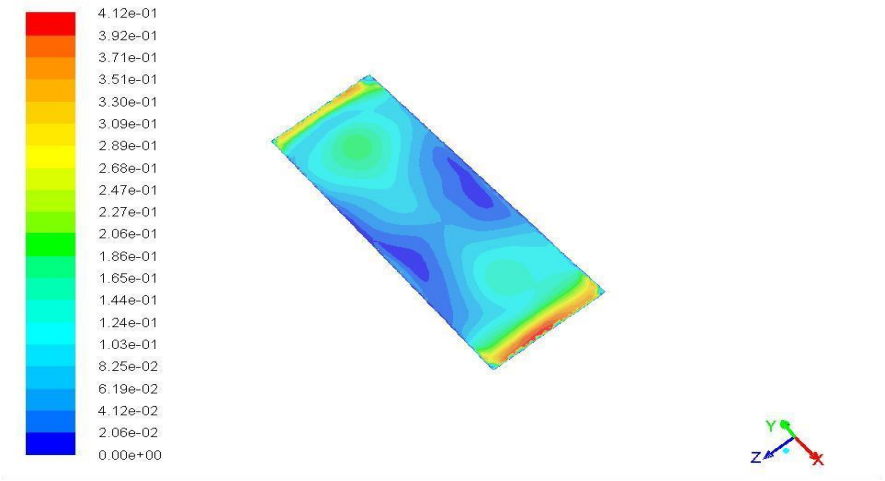

b

Figure 6. The flow velocity pattern for operating conditions B at (a) iso-surface Z=0.56 m (b) iso-surface Y=0.5 m

4.2 Water phase volume fraction contour

The volume fraction contours of the water phase in the desalter are illustrated in Figures 7 and 8, which show the phase separation is made as well. Because this desalter is an electrostatic field with DC current type, the droplets are charged after collision with the electrode due to their fixed and one-way nature, when moving towards the opposite electrode. The volume fraction of water droplets in the space between the two electrodes and near the electrode plates is more than the other parts, Figures 7 and 8, indicating the role of the electrostatic field with the DC current in sticking the water droplets together in the water phase of the desalter. Around the electrode plates, the electrostatic forces cause smaller droplets' coalescence and generate larger droplets. Here it is evident that this model is in perfect agreement with the real conditions.

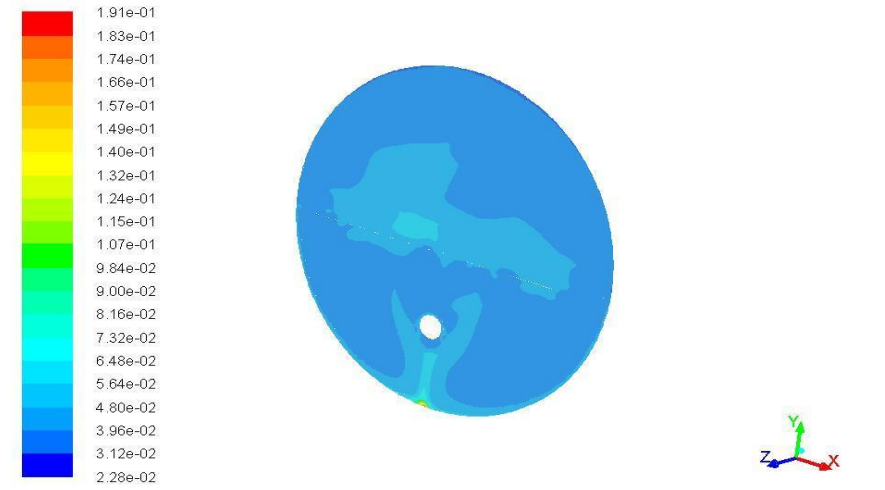

a

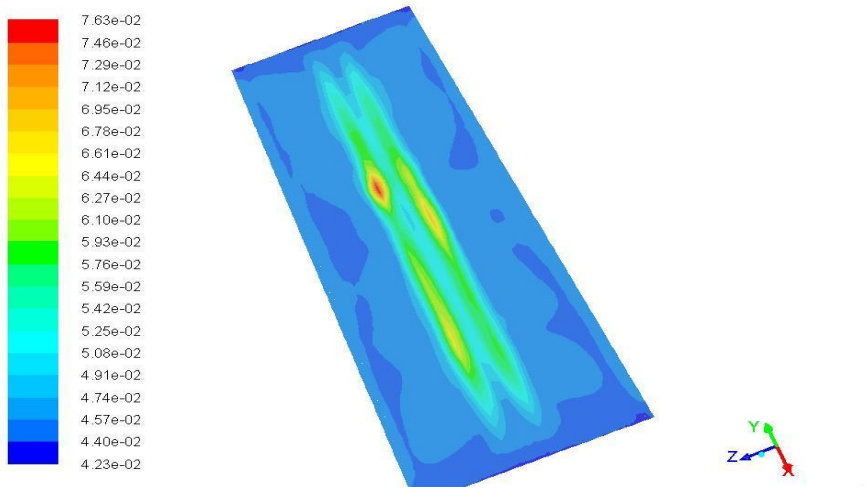

b

Figure 7. The water phase volume fraction contours for operating conditions A at (a) iso-surface Z=0.56 m (b) iso- su rface Y=0.5 m

a

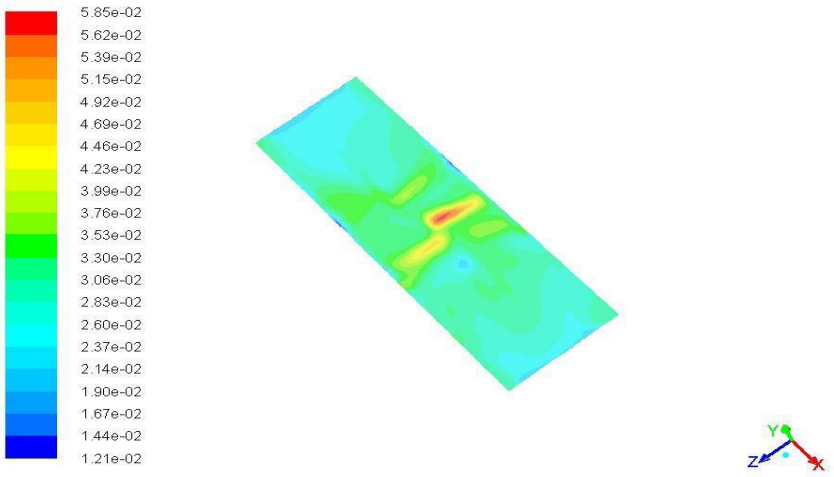

b

Figure 8. The water phase volume fraction contours for operating conditions B at (a) iso-surface Z=0.56 m (b) iso- surface Y=0.5 m

4.3 Droplet size distribution

To better illustrate the droplet size distribution, a few different locations in the desalter are selected. These locations are shown in Figure 9, and their coordinates are tabulated in Table 7, tagged with numbers 1, 2, 3, 4, and 5. Point 1 is located in the area under the inlet, which is the region where the water droplets coalescence due to the weight effect, and points 2, 3, 4, and 5 are located in the inlet, in the area between the electrodes, at the outlet, and in the water outlet at the bottom of desalter, respectively.

The distribution of droplets size at points (1) and (2) are shown in Figures 10 and 11 for both operating conditions A and B, respectively, where, the percent of smaller groups are decreased, and larger-sized groups gain value; thus, the coalescence of droplets in region 1 is important due to coalescence of the droplets in the electrostatic field in the upstream area and fall due to their weight. As it is known, the reduction in the droplet size is low and as the electric field is lower than the critical electric field; therefore, the droplet breakage in the total desalter is ignored.

The droplets size distribution at point (3) is shown in Figures 12 and 13 for operating conditions A and B, respectively, where, the applied electrostatic field in this region increases the collision of droplets; therefore, here, the droplet size especially the larger droplets, increase. The droplet size distribution at point (4) is indicated in Figures 14 and 15 for operating conditions A and B, respectively. Comparison of the distribution results at the outlet of condensate with droplet size distribution at the inlet reveals that, due to the low volume of water present in the condensate outlet, the largest share of the distribution of size groups is related to smaller size groups where the electric field cannot coalesce them and could not fall because of their low weight. The droplet size distribution at point (5) as shown in Figures 16 and 17, larger droplets of 500 µm have a significant volume fraction in the water outlet, which falls due to their weight and exit from the water outlet.

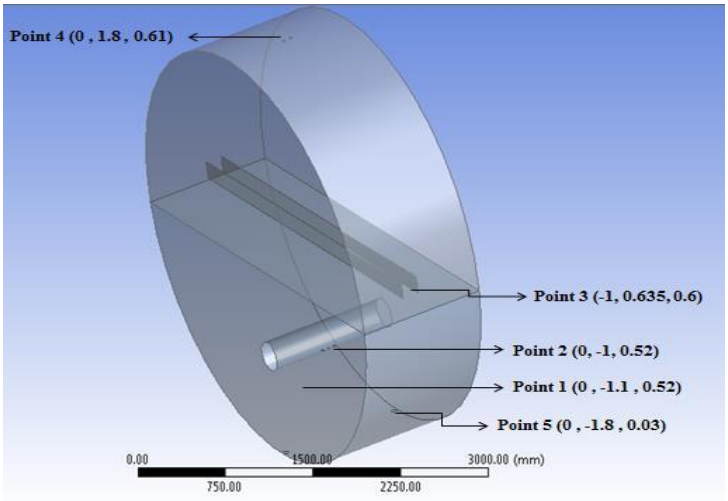

Figure 9. The selected locations in the desalter for studying changes in droplet size distribution

Table 7. The coordinates of points for studying changes in droplet size distribution in the desalter

Point	Coordinates (m)
1	(0, -1.1, 0.52)
2	(0, -1, 0.52)
3	(-1, 0.635, 0.6)
4	(0, 1.8, 0.61)
5	(0, -1.8, 0.03)

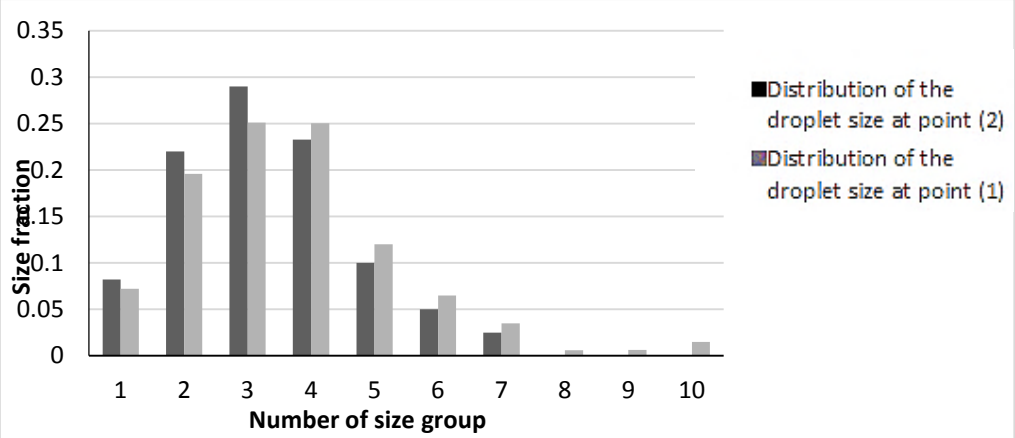

Figure 10. The droplets size distribution at points 1 and 2 for operating conditions A

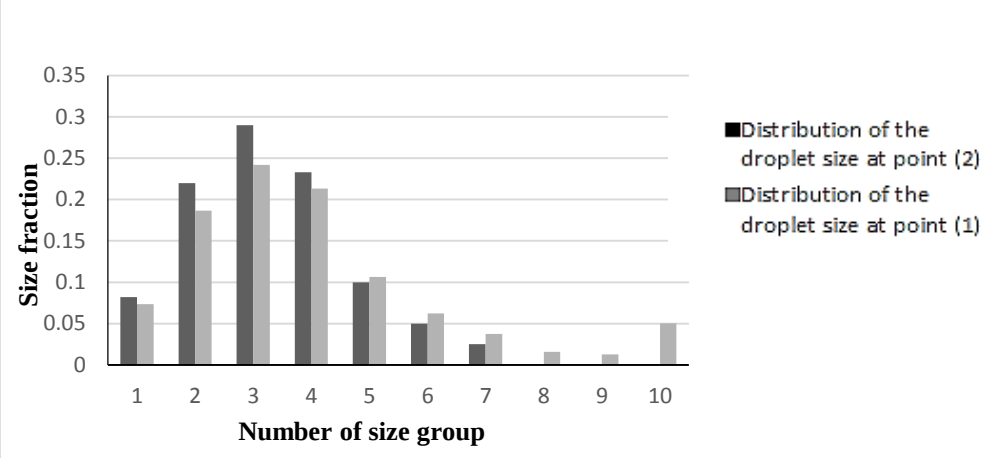

Figure 11. The droplets size distribution at points 1 and 2 for operating conditions B

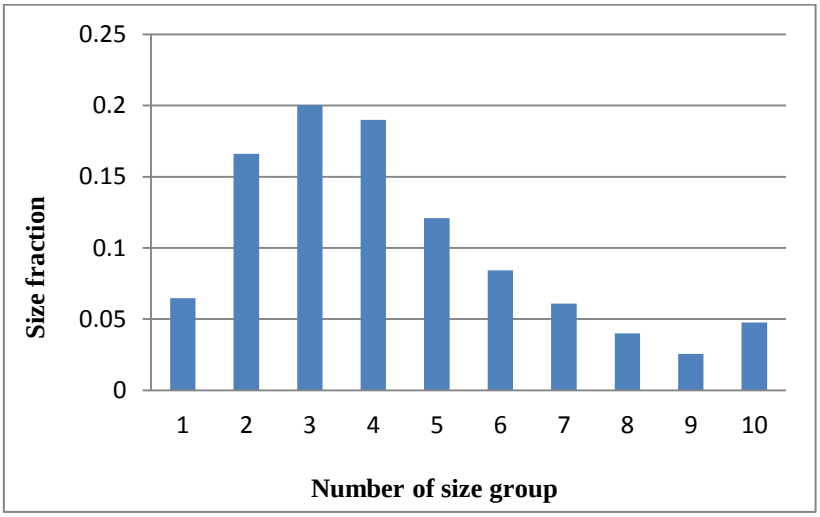

Figure 12. Distribution of droplet size at point 3 for operating conditions A

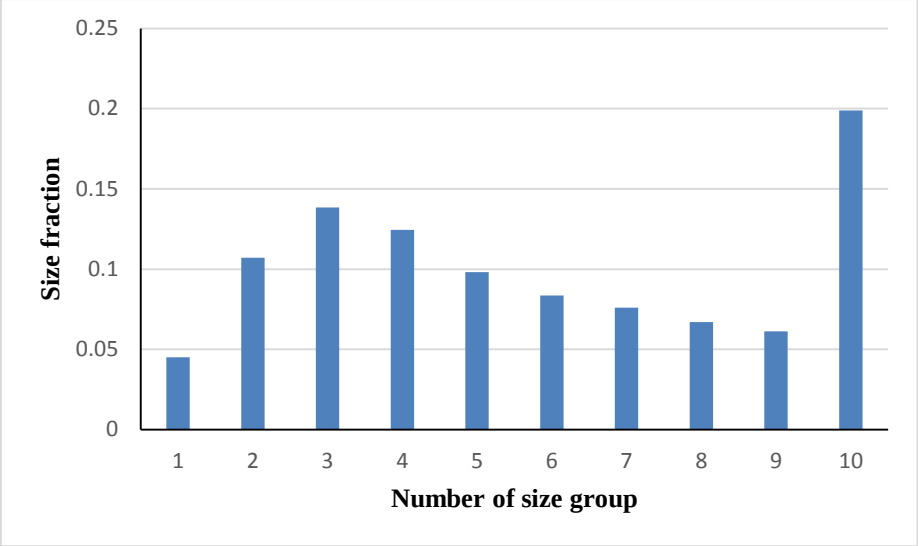

Figure 13. Distribution of droplet size at point 3 for operating conditions B

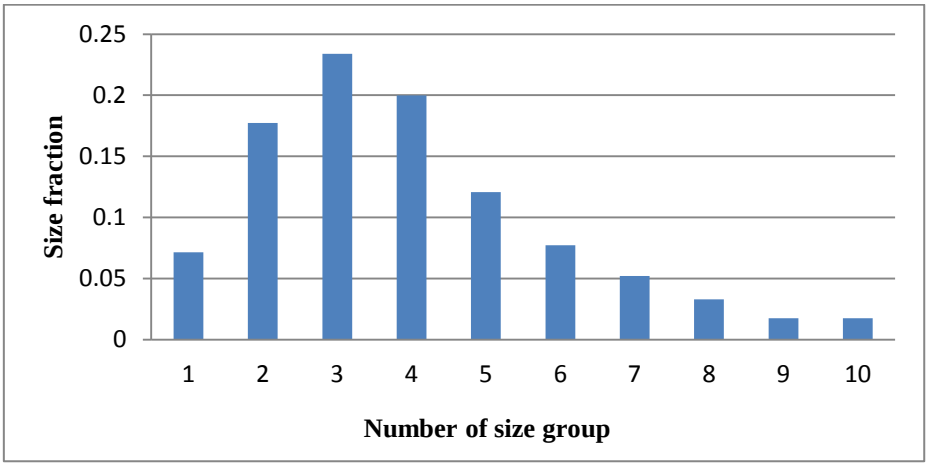

Figure 14. Distribution of droplet size at point 4 for operating conditions A

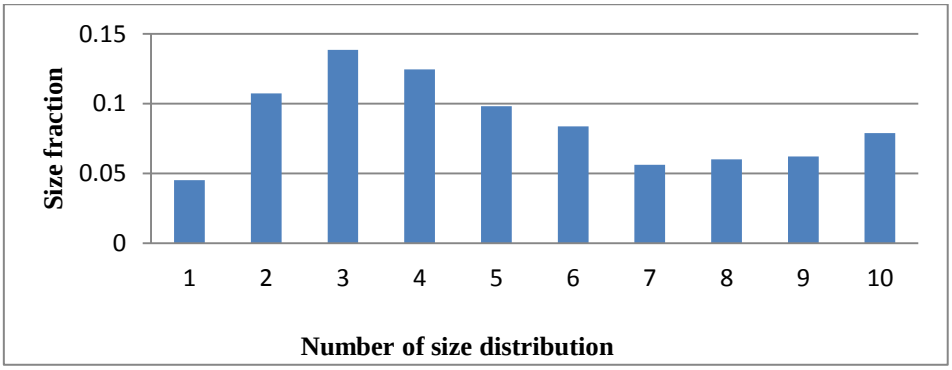

Figure 15. Distribution of droplet size at point 4 for operating conditions B

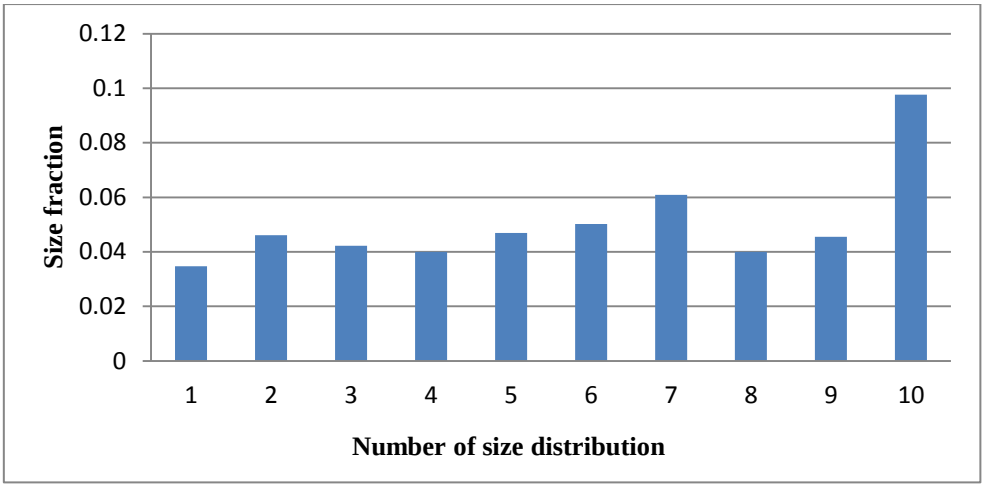

Figure 16. Distribution of droplet size at point 5 for operating conditions A

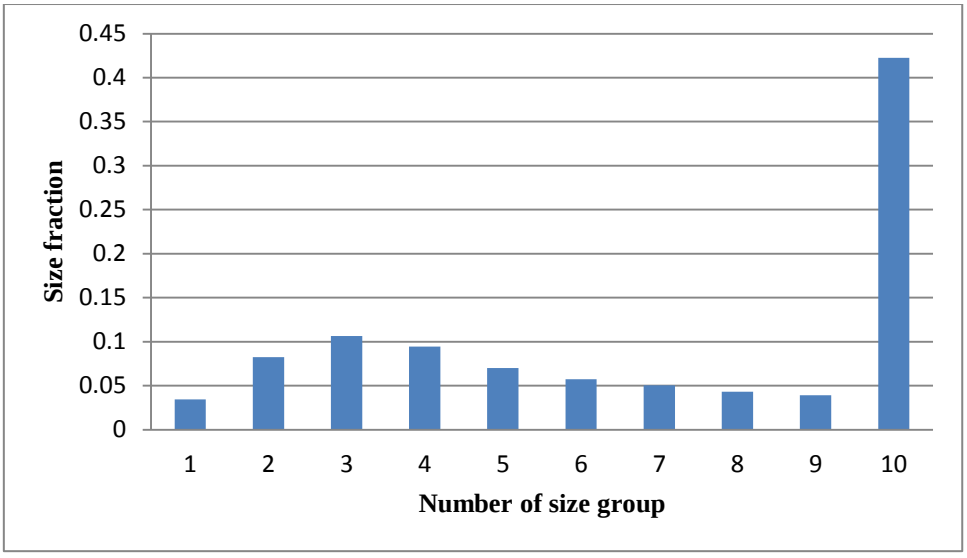

Figure 17. Distribution of droplet size at point 5 for operating conditions B

5. Conclusions

A 3D CFD simulation along with industrial data was run to predict the performance of an electrostatic desalter in Refinery No.4 of South Pars, Iran. The electrostatic desalter was simulated based on the Eulerian-Eulerian method. To consider the coalescence of the water droplets in the population balance model, due to the presence of an electric field a UDF was written and compiled into the ANSYS Fluent 16 S/W.

The volume fraction was calculated through simulation as the main measure of water separation from gas condensate and validated through the industrial data. The computational errors for the operating conditions A and B were 2.5 and 11.9 %, respectively, indicating the accuracy of the simulation.

The flow velocity pattern in both operating conditions at the inlet is disturbed and rotating, and circles around the inlet and fills the total desalter space. Furthermore, a maximum velocity range is established between the plates, indicating the accuracy of this simulation.

Moreover, according to the dispersed phase volume fraction pattern, in the space between the two electrodes and around the electrode plates, the collision of droplets is increased than the other sections indicating the role of the electrostatic field under the DC current established in the coalescence of water phase droplets in the desalter. Around the electrode plates, the electrostatic forces cause smaller droplets to adhere to one another, thus making larger droplets. This model had an acceptable agreement with the real conditions governing the problem.

By comparing water droplets' size distribution results in the outlet of condensates and the inlet, it is revealed that the greatest part of the distribution of size groups belongs to the small size groups where the electric field is unable to coagulate. Due to the applied electric field being lower than the critical electric field of each droplet, the breakage in the total of desalter was ignored. As the droplets size distributed in the

water outlet, the percentage of small size groups was decreased, and the large size groups gain value, indicating that the rate of droplets coagulation in this area is important due to the electrostatic field in the upstream area and its fall due to the weight.

Acknowledgments

The authors would like to thank South Pars Refinery No. 4 for supporting this work.

Notes

The authors declare no competing financial interest. This research did not receive any specific grant from funding agencies in the public, commercial, or not-for-profit sectors.

Nomenclature

$\mathbf{A_p}$	Projected frontal area of the droplet (m^2)
C_L	Lift coefficient
C_{TD}	Dispersion coefficient of turbulence
C_d	Drag coefficient
D	Droplet diameter (m)
$\boldsymbol{E}$	Electric field (V/m)
E_0	Applied electric field of the continuous phase
F_d	Dipole force (N)
F_e	Electrophoretic force (N)
F^{buo}	Buoyancy force (N)
F_d^{td}	Turbulence force of the dispersed phase (N)
F_d^{drag}	Drag force exerted to dispersed phase (N)
F_d^{lift}	Lift force exerted to dispersed phase (N)
K	Empirical coefficient
Q_E	Electric field intensity
Q_{ij}	Characteristic velocity for coalescence of droplets
V_{jk}	Relative velocity of the j and k droplets (m/s)
U_{rel}	Relative velocity between the phases (m/s)
V_{jk}	Relative velocity of the j and k droplets (m/s)
μ_o	Continuous phase viscosity (Pa.s)
ρ	Density (kg/m^3)
ε_1	Dielectric constant of the continuous phase (F/m)
f_i	Dispersed phase fraction for the i-size group
μ_d	Dispersed phase viscosity (Pa.s)
e_{jk}	Droplet collision efficiency
v_v	Droplet velocity (m/s)
λ	Interfacial tension (N/m)
$\boldsymbol{\nu}$	Kinematic viscosity (m^2/s)
ε_O	Oil permittivity coefficient of the continuous phase (F/m)
$\boldsymbol{\sigma}$	Surface tension (N/m)
μ_t	Turbulent viscosity (Pa.s)
ε_0	Vacuum permittivity coefficient (F/m)
μ_o	Viscosity of continuous phase (Pa.s)
α	Volume fraction
ε_w	Water permittivity coefficient (F/m)

References

Eow, J. S., & Ghadiri, M. (2002). Electrostatic enhancement of coalescence of water droplets in oil: a review of the technology. *Chemical Engineering Journal*, *85*(2-3), 357-368. DOI: 10.1016/S1385-8947(01)00250-9

Aryafard, E., Farsi, M., & Rahimpour, M. R. (2015). Modeling and simulation of crude oil desalting in an industrial plant considering mixing valve and electrostatic drum. *Chemical Engineering and Processing: Process Intensification*, *95*, 383-389. DOI: 10.1016/j.cep.2015.06.011

Hosseinpour, F. (2016). Comparison of electrical mixing and mixing valve in the crude oil desalting unit. M. Sc. Thesis. Shahid Bahonar University of Kerman, Iran.

Zhang, X., Basaran, O. A., & Wham, R. M. (1995). Theoretical prediction of electric field-enhanced coalescence of spherical drops. *AIChE Journal*, *41*(7), 1629-1639. DOI: 10.1002/aic.690410704

Berg, G., Lundgaard, L. E., Becidan, M., & Sigrnond, R. S. (2002, July). Instability of electrically stressed water droplets in oil. In *Proceedings of 2002 IEEE 14th International Conference on Dielectric Liquids. ICDL 2002 (Cat. No. 02CH37319)* (pp. 220-224). IEEE.

Zeidani, K., & Bahadori, A. (2008). New equations predicting the best performance of electrostatic desalter. *Petroleum science and technology*, *26*(1), 40-49. DOI: 10.1080/10916460600705634

Meidanshahi, V., Jahanmiri, A., & Rahimpour, M. R. (2012). Modeling and optimization of two stage AC electrostatic desalter. *Separation Science and Technology*, *47*(1), 30-42. DOI: 10.1080/01496395.2011.614316

Mhatre, S., & Thaokar, R. (2015).

Electrocoalescence in non-uniform electric fields: An experimental study. *Chemical Engineering and Processing: Process Intensification*, *96*, 28-38. DOI: https://doi.org/10.1016/j.cep.2015.07.025

Aryafard, E., Farsi, M., Rahimpour, M. R., & Raeissi, S. (2016). Modeling electrostatic separation for dehydration and desalination of crude oil in an industrial two-stage desalting plant. *Journal of the Taiwan Institute of Chemical Engineers*, *58*, 141-147. DOI: 10.1016/j.jtice.2015.06.028

Rossi, F., Colombo, S., Pierucci, S., Ranzi, E., & Manenti, F. (2017). Upstream operations in the oil industry: rigorous modeling of an Electrostatic Coalescer. *Engineering*, *3*(2), 220-231. DOI: 10.1016/J.ENG.2017.02.013

Ramirez-Argaez, M. A., Abreú-López, D., Gracia-Fadrique, J., & Dutta, A. (2021). Numerical Study of Electrostatic Desalting Process Based on Droplet Collision Time. *Processes*, *9*(7), 1226. DOI: 10.3390/pr9071226

Ranaee, E., Ghorbani, H., Keshavarzian, S., Abarghoei, P. G., Riva, M., Inzoli, F., & Guadagnini, A. (2021). Analysis of the performance of a crude-oil desalting system based on historical data. *Fuel* , *291*, 120046. DOI: https://doi.org/10.1016/j.fuel.2020.120046

Dhandhi, Y., Chaudhari, R. K., & Naiya, T. K. (2022). Development in separation of oilfield mulsion toward green technology–A comprehensive review. *Separation Science and Technology*, *57*(10), 642-1668. DOI: https://doi.org/10.1080/01496395.2021.1995427

Ahmadi, S., Khormali, A., & Khoutoriansky, F. M. (2022). Optimization of the demulsification of water-in-heavy crude oil emulsions using response surface methodology. *Fuel*, *323*, 124270. DOI: https://doi.org/10.1016/j.fuel.2022.124270

Versteeg, H. K., & Malalasekera, W. (2007). *An introduction to computational fluid dynamics: the finite volume method*. Pearson education. New York: Longman Group.

White, F. M., & Majdalani, J. (2006). *Viscous fluid flow* (Vol. 3, pp. 433-434). New York: McGraw-Hill.

Soo, S. L. (2018). *Particulates and continuum: multiphase fluid dynamics*. Routledge. DOI: https://doi.org/10.1201/9780203744291

ANSYS Fluent 16 User's Guide, ANSYS, Ltd., (2006).

Coulaloglou, C. A., & Tavlarides, L. L. (1977). Description of interaction processes in agitated liquid-liquid dispersions. *Chemical Engineering Science*, *32*(11), 1289-1297. DOI: 10.1016/0009-2509(77)85023-9

Sadeghi, R., Mohebbi, A., & Baniasadi, M. (2011). CFD modeling of the launder of settler of an industrial copper solvent extraction plant: A case study on Sarcheshmeh copper complex, Iran. *International Journal of Mineral Processing*, *98*(1-2), 55-65. DOI: 10.1016/j.minpro.2010.10.009

Sadeghi, R., Mohebbi, A., Sarrafi, A., Soltani, A., Salmanzadeh, M., & Daneshpojooh, S. (2011). CFD simulation and optimization of the settler of an industrial copper solvent extraction plant: A case study. *Hydrometallurgy*, *106*(3-4), 148-158. DOI: 10.1016/j.hydromet.2010.12.010

Kakhki, N. A., Farsi, M., & Rahimpour, M. R. (2016). Effect of current frequency on crude oil dehydration in an industrial electrostatic coalescer. *Journal of the Taiwan Institute of Chemical Engineers*, *67*, 1-10. https://doi.org/10.1016/j.jtice.2016.06.021